PCCP

ROYAL SOCIETY OF CHEMISTRY

PAPER

View Article Online
View Journal | View Issue

Cite this: *Phys. Chem. Chem. Phys.*, 2023, **25**, 17434

Experimental and theoretical investigation on the anti-corrosion characteristics of pyridine-substituted benzothiazole derivatives for mild steel in aqueous HCl†

Aditya Suhasaria,[a] Rakhi Senapati,[a] Sanjoy Satpati,[b] Subhas Ghosal,[a] Sukalpa Dey[c] and Dipankar Sukul *[a]

Received 27th March 2023,
Accepted 13th June 2023

DOI: 10.1039/d3cp01392h

rsc.li/pccp

Three new 2-(2-pyridyl)benzothiazole derivatives, namely 2-(benzothiazol-2-yl)pyridin-3-amine (APYBT), 2-(benzothiazol-2-yl)pyridin-5-ol (HPYBT) and 2-(pyridin-2-yl)benzothiazole (PYBT), have been synthesized. Those are tested for their potentiality to impart corrosion resistance to mild steel exposed to 1 M aqueous HCl. Both electrochemical and gravimetric experiments establish the studied benzothiazole (BT) derivatives as promising corrosion inhibitors, with APYBT standing out as the most effective one exerting more than 97% inhibition efficiency at 1 mM concentration. PYBT exerts the least inhibitory performance. The electron donating property of the amine group present on the pyridine moiety in APYBT could be responsible for the superiority of APYBT as a corrosion inhibitor among the three. A potentiodynamic polarization study revealed that the inhibitors could retard both the cathodic and anodic reactions. The adsorption of the inhibitors on metal surfaces follows the Langmuir adsorption isotherm. SEM images provide visual confirmation of the protection of mild steel surfaces from corrosion in the presence of the studied benzothiazole (BT) derivatives. The interaction pattern between the mild steel and the inhibitors is explored using results derived from density functional theory (DFT) calculations. Variation of the interaction energy as obtained from molecular dynamics (MD) simulation confirms the corrosion inhibitory trend. Fukui index calculation enables the role played by the substituent group towards the relative electron donation/acceptance properties of the atoms present at the different parts of the inhibitor molecule.

Introduction

Corrosion leads to the deterioration of a material, resulting from its chemical reaction with the environment. Metals thus adopt a more stable form, such as oxide, hydroxide, or sulphide. Corrosion leads to the degradation of various desirable properties of materials and shortens their shelf-life. However, as corrosion is thermodynamically spontaneous, only preventive measures can be employed. In addition to various other methods, like cathodic protection, the application of a corrosion inhibitor is another cost-effective and practical method. Suitable organic inhibitors by virtue of the presence of π-bonds and lone electron pairs on the heteroatoms, like N, O and S, are adsorbed on the metal surface and block the cathodic or anodic reaction sites, or both.[1–9] However, due to their environmentally harmful effects, heavy metal-based inorganic corrosion inhibitors are now under a process of gradual replacement with relatively environmentally benign organic inhibitors. A recent report showed that a mixture of rare earth metal ions, like Ce^{3+}, in conjugation with amino acids, like cysteine, provides remarkable resistivity to corrosion of Al alloys in a saline environment.[10] In recent years, there has been a tremendous surge in research employing various categories of organic corrosion inhibitors. This includes different heterocyclic bases, like thiazoles, benzothiazoles, benzotriazoles, imidazoles, benzimidazoles, benzoxazoles and many others.[11–16] The examination of corrosion protection for mild steel in acidic environments is of primary interest among the researchers in this field. Steel is the most important structural and engineering material. High compressive and tensile strength, ductility and weldability, malleability, and above all relatively low cost

[a] *Department of Chemistry, National Institute of Technology, Durgapur 713 209, India. E-mail: dipankar.sukul@ch.nitdgp.ac.in*
[b] *Department of Chemistry, Government General Degree College, Tehatta, Nadia 741 160, India*
[c] *Department of Basic Science and Humanities, Dr B. C. Roy Engineering College, Durgapur 713 206, India*

† Electronic supplementary information (ESI) available: NMR, FTIR, mass spectra, EIS spectra, adsorption isotherms, Arrhenius plots, and Fukui indices. See DOI: https://doi.org/10.1039/d3cp01392h

have made mild steel the most in-demand material in industry.[17] Mild steel is susceptible to corrosion, and its severeness is enhanced in acidic and saline environments. During acid treatment in different applications (mostly using hydrochloric and sulphuric acid), like pickling, ore production, and gas/oil well acidizing, corrosion inhibitors are essential to combat the menace of corrosion of mild steel.

In the present work, we have dealt with an important class of heterocyclic scaffolds containing a benzothiazole ring system. Benzothiazoles are well-known for biological applications, as well as in material science.[18–23] The presence of multiple functionalities and easy provision for derivatization has enabled a variety of BT derivatives to be obtained for versatile applications. There are many reports on 2-substituted BT derivatives as corrosion inhibitors, like 2-amino BT, 2-mercapto BT and others.[24,25] Some researchers have reported anti-corrosive performance of 6-substituted 2-amino BT derivatives.[26–28] More structurally complicated 2-substituted BT derivatives, prepared through multistep synthesis, or BT derivatives substituted at both 2 and 6-positions have also been reported in order to obtain better inhibition efficiency.[29,30] In the present work, we have designed a structurally very simple inhibitor, 2-pyridine benzothiazoles, in a single step synthesis. In addition, to elucidate the effect of an electron donating group on the overall corrosion inhibition, we prepared two other molecules where aminopyridine and hydroxypyridine groups are attached at the 2-position of BT. Generally, pyridine derivatives with electron withdrawing and electron donating substituents showed a better anticorrosion effect than that of the native pyridine.[31–37] Pyridine derivatives containing polar substituents form highly stable chelating complexes, which may be the cause for such better performance.[38] In this present work, we have employed detailed electrochemical and gravimetric analysis to elucidate the electronic effects of substituents on the pyridine moiety towards the anti-corrosion behaviour of the synthesized 2-pyridine benzothiazoles (BT-Py). Experimental observations are corroborated with density functional theory (DFT) calculations and molecular dynamics (MD) simulation.

Experimental

Preparation and characterisation of inhibitors

20 mL of polyphosphoric acid (PPA, Sigma-Aldrich) was taken in a 100 mL round bottom flask, then 7.5 mmol of pyridine-2-caboxyllic acid (0.9233 g) (Alfa Aesar), 3-amino pyridine-2-carboxyllic acid (1.063 g) (Alfa Aesar) or 5-hydroxy pyridine-2-carboxyllic acid (1.043 g) (Alfa Aesar) was added in a separate set of experiments and heated under stirring conditions at 120–150 °C until a homogeneous mixture was obtained. Then, to this solution, 7.5 mmol of 2-amino thiophenol (0.9389 g) (Alfa Aesar) was added dropwise and the mixture was allowed to reflux for 24 h under heating conditions (Scheme 1). After the completion of the reaction, as confirmed by TLC, the solution was cooled at room temperature. Then, 10% NaOH was added dropwise until

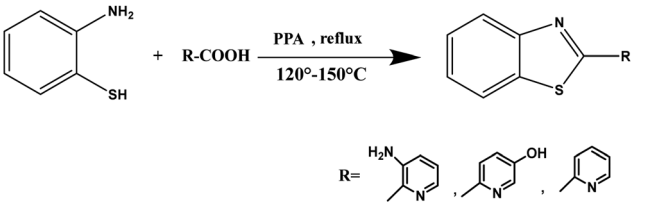

Scheme 1 Schematic diagram of the preparative method of the pyridine-substituted benzothiazole derivatives.

the pH of the mixture was adjusted to 9. The precipitate obtained was filtered out and washed using hot water and aqueous methanol, and finally using diethyl ether. Details of the physical state of the synthesized inhibitors are given in Table 1.

^{1}H NMR analysis of the synthesized benzothiazole derivatives was carried out using a Bruker ASCEND 400 spectrometer in $CDCl_3$ at 400 MHz. An IRA-1S WL (Shimadzu) spectrometer was used for FTIR characterization. ESI mass spectra were recorded in an Agilent ESI mass spectrometer.

(A) ^{1}H NMR in $CDCl_3$ at 400 MHz (Fig. S1(A–C) in ESI†)

APYBT. δ (ppm) 8.09–8.10 (1H, d, α-H of py-ring), 8.01–8.03 (1H, d, Ar-H), 7.94–7.97 (1H, d, Ar-H), 7.49 (1H, t, Ar-H), 7.40 (1H, t, Ar-H), 7.18 (1H, t, β-H of py-ring), 7.14 (1H, d, γ-H of py-ring), 6.37 (2H, s, $-NH_2$ group).

HPYBT. δ (ppm) 8.26–8.27 (1H, d, α-H of py-ring), 8.18–8.21 (1H, d, δ-H of py-ring), 8.09–8.11 (1H, d, Ar-H), 8.01–8.04 (1H, d, Ar-H), 7.52 (1H, t, Ar-H), 7.43 (1H, t, Ar-H), 7.36–7.38 (1H, d–d, γ-H of py-ring).

PYBT. δ(ppm) 8.71–8.72 (1H, d, α-H of py-ring), 8.41–8.39 (1H, d, δ-H of py-ring), 8.10–8.13 (1H, d, Ar-H), 7.97–8.00 (1H, d, Ar-H), 7.87 (1H, t, γ-H of py-ring), 7.53 (1H, t, Ar-H), 7.44 (1H, t, Ar-H), 7.40 (1H, d–d, β-H of py-ring).

(B) Mass spectrum (Fig. S2 in ESI†)

The appearance of very strong and sharp peaks at m/z 227 (Fig. S2A) and 228 (Fig. S2B), ESI† in the EI-mass spectrum confirms the formation of APYBT and HPYBY, respectively.

The appearance of a strong molecular ion peak at m/z 213.049 (100%) in the ESI-mass spectrum (Fig. S2C, ESI†) confirms the formation of PYBT.

(C) FTIR (Fig. S3 in ESI†)

The appearance of peaks in the range of 1566–1605 cm^{-1} in the corresponding FTIR spectra of the synthesized BT-Py derivatives confirmed the formation of C═N in the benzothiazole ring. Strong and sharp peaks in the regions of 1432–1460 cm^{-1} and 747–756 cm^{-1} indicate the presence of C–N and C–S stretching vibrations, respectively.

Surface preparation of mild steel coupons

Commercially available mild steel coupons having wt% composition 0.19 C, 0.21 Si, 0.21 Mn, 0.01 P, 0.01 S and the remainder iron were polished using different grit size SiC paper

Table 1 Structure, molecular weight and abbreviation of the pyridine-substituted benzothiazole derivatives

Molecular name (abbreviation)	Molecular structure	Mol. wt.	Physical state
(Benzothiazol-2-yl)pyridin-3-amine (APYBT)	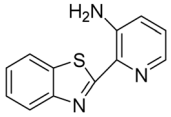	227.28	Yellow amorphous solid
2-(Benzothiazol-2-yl)pyridin-5-ol (HPYBT)	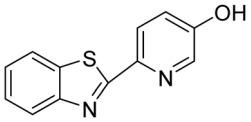	228.27	White amorphous solid
2-(Pyridin-2-yl)benzothiazole (PYBT)	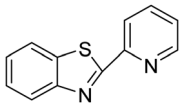	212.27	White amorphous solid

of 60 to 1200. The coupons were then washed using soap water and distilled water, and dried with acetone followed by rubbing the surface using a velvet cloth.

Experimental measurements

Electrochemical techniques such as potentiodynamic polarization and electrochemical impedance spectroscopic studies (employing an ACM electrochemical workstation, model: GILL AC, UK) were implemented using the conventional three electrode system with a mild steel coupon, saturated calomel electrode (SCE) and platinum mesh electrode being used as the working, reference and auxiliary electrodes, respectively. A surface area of 0.5 cm^2 was exposed to 350 mL of acid solution. Before the electrochemical experiments, the surface of the working electrodes was kept in contact with the test solution for 45 min until a steady potential was reached. Open circuit potential (OCP) was observed for the next 5 min. The results are depicted in Fig. 1, which shows almost no variation in the potential value, confirming the attainment of the steady state.

Potentiodynamic polarization plots were acquired by changing the electrode potential in the range of ±250 mV from OCP with a constant sweep rate of 0.5 mV s^{-1}. Percentage inhibition efficiency (η_P) is obtained by the following relation:

$$\eta_P(\%) = \frac{i_{corr} - i_{corr(inh)}}{i_{corr}} \times 100 \quad (1)$$

where i_{corr} and $i_{corr(inh)}$ are the corrosion current density for the uninhibited and inhibited system, respectively.

Electrochemical impedance measurements were done in the frequency range of 100 kHz to 0.01 Hz with an amplitude of ±10 mV using the AC signal at OCP. Using this method, the inhibition efficiency is calculated as:

$$\eta_Z(\%) = \frac{R_p - R_p^0}{R_p} \times 100 \quad (2)$$

where R_p and R_p^0 stand for the polarisation resistance values of the inhibited and uninhibited system, respectively.

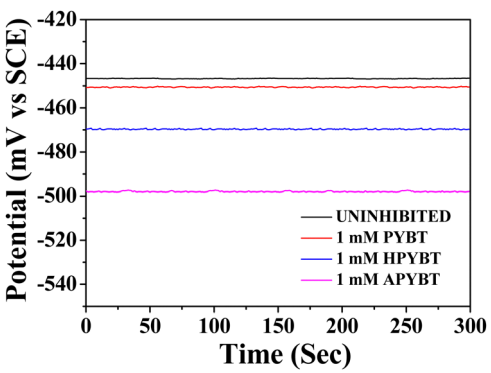

Fig. 1 Variation of the open circuit potential of mild steel with time after 45 minutes in contact with 1 M HCl in the absence and presence of 1 mM concentration of inhibitors at 30 °C.

Weight-loss measurement

Cleaned and pre-weighed mild steel specimens of dimensions 2.5 cm × 2.5 cm × 0.1 cm were immersed in 100 mL of test solution at different temperatures (20–50 °C) and for different time durations (6–96 h). After a specific time span, the mild steel specimens were taken out from the acid solution and washed under flowing water to remove the rust (using bristled brass when required). The specimens were then washed with acetone, dried under vacuum and again weighed. From the average weight losses, the inhibition efficiencies were calculated using the following relation:

$$\eta_W(\%) = \frac{W_0 - W}{W_0} \times 100 \quad (3)$$

where W and W_0 are the values of the weight loss with and without the addition of the inhibitor, respectively.

All electrochemical and gravimetric experiments were done in triplicate and the average value is shown here.

Surface morphology

To compare the surface morphologies of the uninhibited and inhibited corroded samples after immersion in the acid solution for 24 h, scanning electron microscopy (SEM) images were taken using a Hitachi S-3000N microscope.

Computational details for quantum chemical calculation

To analyze the correlation between the inhibitors' electronic properties and their corresponding inhibition efficiencies, quantum chemical calculations were done using density functional theory (DFT) using the B3LYP functional and double numeric with polarization (DNP) basis set (DMol3 module of Materials studio 2020) employing an energy convergence of 10^{-6} Ha and displacement convergence of 5×10^{-3} Å. A dielectric constant of 78.54 is used to model the water environment during the calculation of the electronic parameters.[39,40]

Numerous intrinsic molecular parameters, like electron affinity (A), ionization potential (I), electronegativity (χ, measures the ability of a group of atoms to attract electrons towards itself), global hardness (η, measures the resistance of an atom towards charge transfer) and global softness (σ, which shows the reactivity of the inhibitor molecules towards charge transfer), were calculated using the following equations.[39–45]

$$\chi = (I + A)/2 \quad (4)$$

$$\eta = (I - A)/2 \quad (5)$$

$$\sigma = 1/\eta = 2/(I - A) \quad (6)$$

$$I = -E_{\mathrm{HOMO}} \quad (7)$$

$$A = -E_{\mathrm{LUMO}} \quad (8)$$

From these values, the fraction of total electron transfer from the inhibitor molecule to the mild steel surface (ΔN) is evaluated using the following relation:[39–45]

$$\Delta N = \frac{(\chi_{\mathrm{Fe}} - \chi_{\mathrm{inh}})}{2(\eta_{\mathrm{Fe}} + \eta_{\mathrm{inh}})} \quad (9)$$

ΔN is based on the concept of interaction between the metallic surface and an inhibitor molecule, which assumes that the electrons will flow from the molecule of lower to one with higher electronegativity until the chemical potentials equalize. In order to calculate ΔN, the electronegativity of Fe (χ_{Fe}) was replaced by the work function of the Fe (1 1 0) surface (ϕ_{Fe}) and was taken as 4.82 eV.[39,40,45] The global hardness of iron, η_{Fe}, was taken as zero considering $I = A$ for the metallic bulk.[39,40,45]

Local reactivity analysis

As an integral part of DFT calculations, the local reactivity of the atoms present in inhibitor molecules was ascertained in terms of the corresponding Fukui indices.[46–48] The Fukui function is elucidated as the first derivative of the electronic density $\rho(r)$ with respect to the number of electrons N at a constant external potential v:

$$f(r) = \left(\frac{\partial \rho(r)}{\partial N}\right)_v \quad (10)$$

When charge transfer occurs during a chemical interaction, electron density changes at a given position (r) for the change in number of electrons, and this is quantified in the above expression.

Extending the concept, condensed Fukui functions (or Fukui indices) of the k-th atom for nucleophilic and electrophilic attacks (f_k^+ and f_k^-, respectively) based on the finite difference approximation[46–48] are given by

$$f_k^+ = q_k(N + 1) - q_k(N) \quad (11)$$

$$f_k^- = q_k(N) - q_k(N - 1) \quad (12)$$

where $q_k(N + 1)$, $q_k(N)$ and $q_k(N - 1)$ are the charges on the k-th atom of the molecule in its anionic (when an electron is added to the LUMO of the molecules), neutral and cationic (when an electron is removed from the HOMO of the molecule) state, respectively.

Molecular dynamics simulation

One inhibitor molecule, 500 water molecules, and 10 each of H_3O^+ and Cl^- ions were annealed within a simulation box with Fe (1 1 0) planes with $20 \times 20 \times 10$ (length × breadth × depth) Fe atoms and a vacuum slab. The total dimension of the box was 49.647 Å × 49.647 Å × 98.241 Å with periodic boundary conditions. MD simulation was performed with the COMPASSIII force field (Materials studio 2020) for 1 ns with a time step of 1.0 fs at 25 °C considering canonical ensemble (NVT) and Berendsen thermostatic conditions. The interaction energy ($E_{\mathrm{interaction}}$) between the inhibitor molecule and Fe surface is calculated as

$$E_{\mathrm{interaction}} = E_{\mathrm{total}} - \left(E_{\mathrm{surface+H_2O+H_3O^+ + Cl^-}} + E_{\mathrm{inhibitor}}\right) \quad (13)$$

where E_{total} is the total interaction energy of the simulated system, $E_{\mathrm{surface+H_2O+H_3O^+ + Cl^-}}$ is the energy of the same system without the inhibitor and $E_{\mathrm{inhibitor}}$ is the energy of the bare inhibitor within the blank simulation box.[49,50]

Results and discussion

Polarization measurements

Fig. 2 depicts the cathodic and anodic polarisation curves of mild steel in 1 M HCl with different concentrations of inhibitors. The corresponding electrochemical parameters such as anodic and cathodic Tafel slopes (b_a and b_c), corrosion current density (i_{corr}) and corrosion potential (E_{corr}) are tabulated in Table 2. The data in the table show that in the absence of any inhibitor, i_{corr} is very high and it gradually decreases in the presence of the inhibitors following the order: PYBT > HPYBT > APYBT. Thus, the inhibition efficiency is highest with APYBT (97% at 1 mM concentration at 30 °C). The decrease in i_{corr} with the increase in inhibitor concentration is attributed to better coverage of the cathodic and anodic reaction sites at higher concentration.[51–53] This results in reduction of both the cathodic and anodic current densities compared to the uninhibited solution (Fig. 2). However, it is seen that the reduction in cathodic current density is relatively more prominent and regular with inhibitor concentration, compared to that of the anodic current density. In the presence of inhibitors, the corrosion potential shifts towards more negative values from that for the uninhibited sample

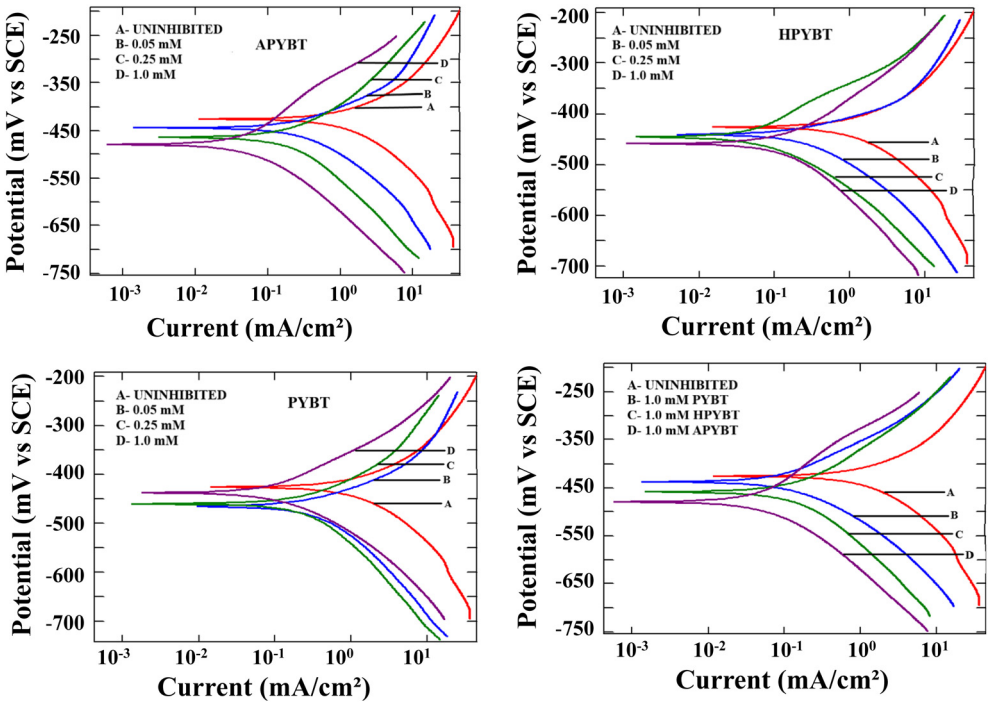

Fig. 2 Potentiodynamic polarization plots for mild steel in 1 M HCl in the presence of various concentrations of inhibitors at 30 °C.

Table 2 Potentiodynamic polarization data for mild steel in 1 M HCl in the presence and absence of inhibitors at 30 °C

Inhibitor	Conc. (mM)	$-E_{corr}$ (mV SCE^{-1})	b_a (mV dec^{-1})	$-b_c$ (mV dec^{-1})	i_{corr}[a] (μA cm^{-2})	η_P (%)
Uninhibited		428	118	133	1703	—
APYBT	0.01	440	97	106	807	52.6
	0.05	445	88	99	341	79.9
	0.10	465	82	93	187	89.0
	0.25	464	82	89	139	91.9
	0.50	439	81	90	74	95.7
	1.00	478	95	102	49	97.1
HPYBT	0.01	437	106	118	1100	35.4
	0.05	441	86	96	480	71.8
	0.10	466	86	94	260	84.7
	0.25	448	104	115	169	90.1
	0.50	468	85	94	126	92.7
	1.00	457	83	91	83	95.2
PYBT	0.01	437	107	116	1294	23.9
	0.05	464	100	106	552	67.6
	0.10	458	94	104	349	79.5
	0.25	458	89	96	206	87.9
	0.50	470	94	101	158	90.7
	1.00	440	82	88	115	93.3

[a] Standard error: within ±9%.

(Table 2). In comparison to the uninhibited sample, the cathodic and anodic Tafel slopes tend to decrease in the presence of inhibitors. Here again, the reduction in the cathodic Tafel slope is relatively higher than for the anodic Tafel slope. These experimental observations suggest that the BT-Py derivatives block both the cathodic and anodic reaction sites, thereby reducing the rate of the corresponding reactions. However, this blocking effect is comparatively more effective for the cathodic sites. Hence, we may classify the studied molecules as cathodic inhibitors. Better corrosion inhibitory performance of APYBT over HPYBT can be attributed to the higher electron donation capacity of the amine group present in APYBT compared to that of the –OH substituent present in HPYBT. Lower electronegativity of N than O is the root cause behind the observed trend. PYBT exhibits the lowest inhibitory performance as no such substituent is present.

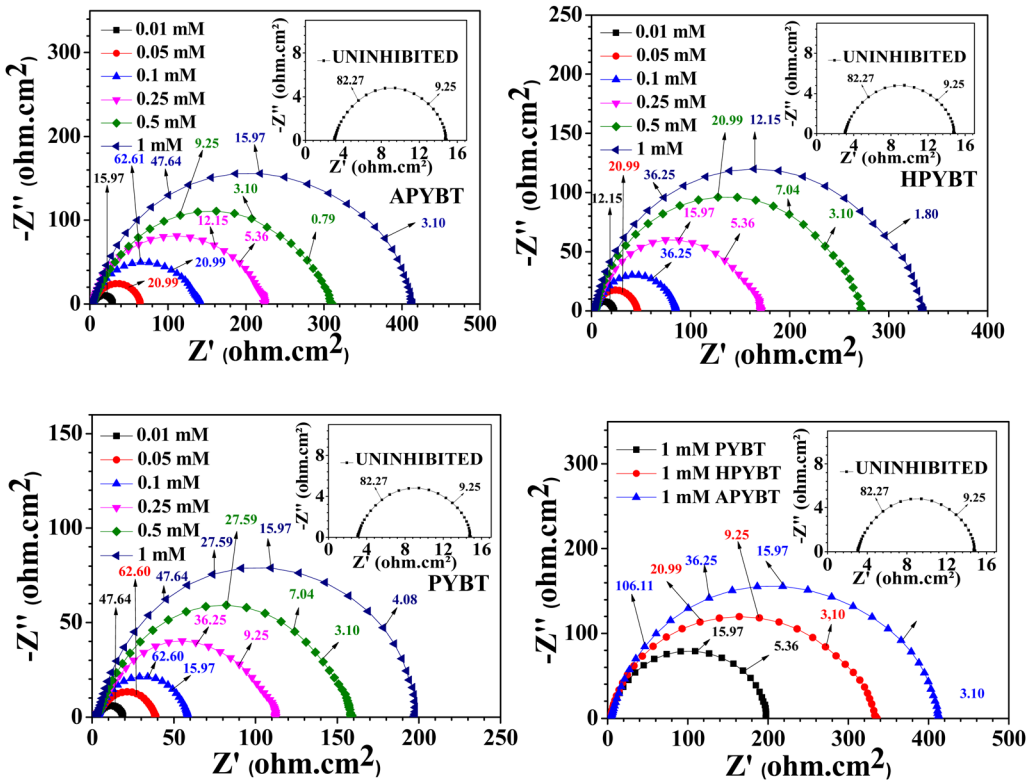

Fig. 3 Nyquist plots for mild steel in 1 M HCl in the presence of BT-pyridine derivatives and comparison at 1 mM concentration at 30 °C.

Electrochemical impedance spectroscopy (EIS)

The mild steel corrosion behaviour in the presence and absence of the inhibitors was investigated using electrochemical impendence spectroscopy. The obtained Nyquist plots are pictured in Fig. 3. The corresponding Bode impedance and phase angle plots at different inhibitor concentrations are shown in Fig. S4(A–C) and S5(A–C) in the ESI.†

The diameter of the capacitive loop in the Nyquist plots increases gradually with increasing inhibitor concentration, which reflects the increase in polarisation resistivity towards charge transfer at the metal–electrolyte interface.[54–56] This demonstrates that the extent of adsorption increases with increasing concentration of the inhibitors. Uninhibited and inhibited systems exhibit one capacitive loop in the Nyquist plots (Fig. 3), while the Bode impedance plots display one negative fluctuation (Fig. S4 in ESI†) and the Bode phase angle plots show only one maximum point (Fig. S5 in ESI†). All of these results correspond to one time constant associated with the charge transfer process. In addition, the capacitive loops are not perfect semi-circles, but rather depressed under the real axis. The phase angles, as exemplified in the Bode phase angle plots, also deviate largely from −90°. These observations correspond to a deviation from ideal capacitive behaviour. To accommodate these deviations, the obtained Nyquist plots are fitted using the equivalent circuit depicted in Fig. 4, where R_p and R_s stand for the polarisation resistance and solution resistance, respectively, and CPE is the constant phase element.[57,58] The impedance of the CPE is given as:

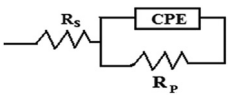

Fig. 4 Equivalent circuit model used to fit the impedance plots.

$$Z_{CPE} = Q^{-1}(i\omega)^{-n} \quad (14)$$

where Q stands for the proportionality coefficient and ω signifies the angular frequency, and n is a measure of surface irregularity. In fact, n can be related with the fractal dimension, D, as:

$$n = 1/(D - 1) \quad (15)$$

For a perfectly smooth surface (*i.e.*, flat two dimensional), $D = 2$, and hence, $n = 1$. Whereas, for a highly contorted surface, (like that of a porous cube), $D = 2$, which yields $n = 0.5$.[59] For a corroded surface exhibiting different extents of surface heterogeneity, the n values lie in-between 0.8 and 1, which is also true in the present case.[60] The surface heterogeneity should result in multiple time constants for the charge transfer process. However, the surface distribution of the time constants is so narrow that experimentally we observe only one time constant.

To illustrate the variation of the double layer capacitance (C_{dl}) with inhibitor concentration, the former is calculated using the Brug equation (eqn (16)), which is derived based on

Table 3 EIS data for mild steel in 1 M HCl in the presence of BT-pyridine derivatives at 30 °C

	Inh. conc. (mM)	R_s (Ω cm^2)	R_p[a] (Ω cm^2)	Q ($\mu\Omega^{-1}$ s^n cm^{-2})	n	C_{dl} (μF cm^{-2})	η_Z%	$\chi^2 \times 10^4$
Inhibitor	Uninhibited	3.1	11.9	816	0.88	349.8	—	8.35
APYBT	0.01	3.7	25.1	242	0.89	99.9	52.6	0.96
	0.05	3.2	61.3	142	0.85	36.2	80.6	1.73
	0.10	3.0	134.1	90	0.84	18.7	91.1	1.55
	0.25	3.1	218.4	59	0.83	10.1	94.6	4.53
	0.50	2.7	306.8	54	0.83	8.8	96.1	3.98
	1.00	2.7	407.9	42	0.84	7.4	97.1	2.76
HPYBT	0.01	1.2	18.9	355	0.89	135.0	37.0	0.68
	0.05	2.6	42.6	196	0.89	76.2	72.1	0.93
	0.10	3.3	81.8	78	0.83	14.2	85.5	0.85
	0.25	2.4	167.7	69	0.83	11.6	92.9	3.72
	0.50	3.2	268.9	65	0.82	10.1	95.6	5.32
	1.00	2.7	334.3	59	0.82	8.6	96.5	2.50
PYBT	0.01	3.4	15.2	268	0.88	100.4	22.4	0.54
	0.05	2.0	35.1	157	0.83	29.7	66.1	4.53
	0.10	2.7	55.1	99	0.86	25.7	78.4	1.24
	0.25	1.9	107.5	109	0.83	19.1	88.9	5.17
	0.50	2.0	153.8	98	0.83	17.0	92.3	5.33
	1.00	1.1	199.2	77	0.85	14.7	94.0	2.41

[a] Standard error: within ± 7%.

the distributed time constant model.[61,62]

$$C_{dl} = Q^{1/n}\left(\frac{R_s R_p}{R_s + R_p}\right)^{(1-n)/n} \quad (16)$$

Following the equation, when n = 1 (which corresponds to the surface being devoid of any kind of imperfection), Q and C_{dl} become equal, *i.e.*, the CPE converts into C_{dl}. All the fitted and calculated parameters are presented in Table 3. The chi squared values (χ^2) listed in Table 3 are on the order of 10^{-4}, indicating the goodness of fitting of the EIS plots.

Table 3 illustrates the gradual increment of the R_p values with the inhibitor concentration, which in turn is reflected in the increasing corrosion inhibition efficiency. The inhibitive performance of the inhibitors follows the order APYBT > HPYBT > PYBT, confirming the observation made in the potentiodynamic polarization study. The C_{dl} values are lowered with enhancement of the inhibitor concentration. Various factors are associated with this: higher surface coverage at higher inhibitor concentration, a decrease in the dielectric constant of the medium at the metal surface due to gradual replacement of the pre-adsorbed water molecules with an organic inhibitor layer, and an increase in the thickness of the inhibitor layer.[39,40] For APYBT, the inhibitor–metal interaction is the most intricate, which results in the maximum decrease in the C_{dl} value as compared to the other two BT-Py derivatives.

Weight-loss measurements

To substantiate the results obtained by electrochemical measurements, weight-loss measurements were done at different temperatures (20–50 °C) and different immersion times for both the uninhibited and inhibited systems (Table 4 and Table S1 in the ESI†). From the obtained data, it is observed that with increasing temperature, the corrosion rate gradually increases.

Table 4 Corrosion rate of mild steel after immersion for 6 h in 1 M HCl in the presence of BT-pyridine derivatives at different temperatures

		Corrosion rate[a] (mg cm^{-2} h^{-1})			η_W (%)		
Temp. (°C)	Inh. conc. (mM)	APYBT	HPYBT	PYBT	APYBT	HPYBT	PYBT
20	0	2.007					
	0.01	0.981	1.335	1.560	51.1	33.5	22.3
	0.05	0.410	0.572	0.735	79.6	71.5	63.4
	0.10	0.205	0.303	0.488	89.8	84.9	75.7
	0.25	0.130	0.195	0.257	93.5	90.3	87.2
	0.50	0.092	0.147	0.185	95.4	92.7	90.8
	1.00	0.070	0.096	0.139	96.5	95.2	93.1
30	0	4.752					
	0.01	2.271	3.103	3.630	52.2	34.7	23.6
	0.05	0.941	1.316	1.696	80.2	72.3	64.3
	0.10	0.461	0.684	1.117	90.3	85.6	76.5
	0.25	0.290	0.432	0.575	93.9	90.9	87.9
	0.50	0.204	0.323	0.409	95.7	93.2	91.4
	1.00	0.152	0.204	0.299	96.8	95.7	93.7
40	0	7.280					
	0.01	3.399	4.667	5.394	53.3	35.9	25.9
	0.05	1.369	1.944	2.512	81.2	73.3	65.5
	0.10	0.641	0.990	1.631	91.2	86.4	77.6
	0.25	0.386	0.604	0.808	94.7	91.7	88.9
	0.50	0.262	0.444	0.561	96.4	93.9	92.3
	1.00	0.189	0.262	0.408	97.4	96.4	94.4
50	0	12.178					
	0.01	5.760	7.903	9.158	52.7	35.1	24.8
	0.05	2.362	3.324	4.287	80.6	72.7	64.8
	0.10	1.132	1.717	2.789	90.7	85.9	77.1
	0.25	0.694	1.072	1.425	94.3	91.2	88.3
	0.50	0.475	0.803	0.999	96.1	93.4	91.8
	1.00	0.341	0.499	0.743	97.2	95.9	93.9

[a] Standard error: within ± 8%.

This is consistent with the fact that corrosion is indeed an activation energy-controlled process, which gets facilitated at

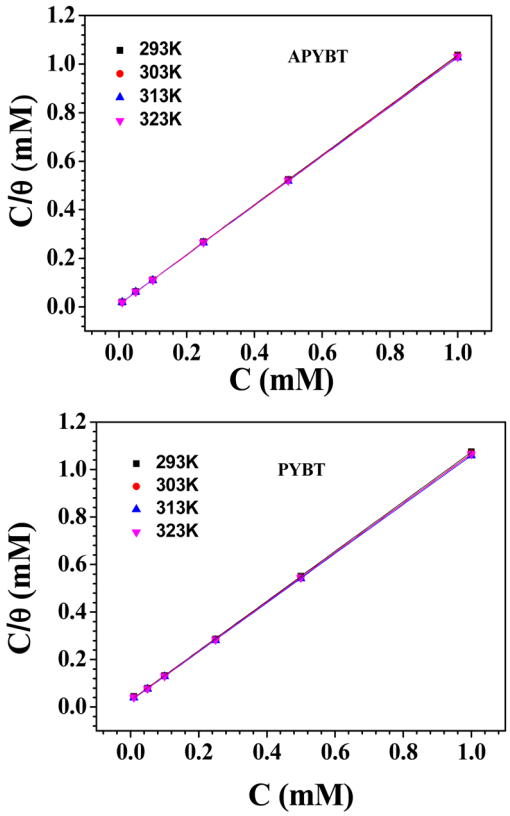

Fig. 5 Langmuir adsorption isotherms of mild steel in 1 M HCl containing APYBT (top) and PYBT (bottom).

elevated temperature. The inhibition efficiency is calculated by comparing the rate of weight loss for the uninhibited and inhibited samples (Table 4). It is revealed to increase from 20 °C up to 40 °C. Beyond 40 °C, the inhibition efficiency shows a retarding tendency. Thus, it may be concluded that BT-Py derivatives provide an effective barrier towards the corrosion of mild steel in acidic environments by the formation of a protective surface layer. However, such an organic layer starts to get damaged above 40 °C. APYBT stands out as a promising corrosion inhibitor for mild steel exposed to 1 M aqueous HCl. It delivers more than 97% inhibition efficiency at 1 mM concentration in the temperature range of 40–50 °C (exposure time of 6 h). Investigation in terms of the effect of the exposure time at 30 °C elucidates that the extent of adsorption and hence the corrosion inhibition efficiency increases with the immersion time and attains the maximum at 48 h (Table S1 and Fig. S9, ESI†). APYBT maintains its potentiality as a corrosion inhibitor by exhibiting an inhibition efficiency well above 96% after the exposure of mild steel to 1 M HCl for 96 h. HPYBT also upholds more than 95% inhibition efficiency under similar experimental conditions. Thus, we can conclude that BT-pyridine derivatives provide a strong and long-lasting protective layer on mild steel surfaces in an acid medium.

Adsorption isotherm study

The efficacy of the studied BT-pyridine derivatives as a successful corrosion inhibitor mainly depends on their ability to get adsorbed on the metal surface. To evaluate the different adsorption parameters, we have correlated the experimentally obtained degree of surface coverage ($\theta = \eta_W(\%)/100$)[63] at a wide range of inhibitor concentrations (C) with different adsorption isotherms. It is found that the experimental data satisfy the most fundamental Langmuir adsorption isotherm quite nicely (eqn (17)). Following this isotherm,

$$\frac{c}{\theta} = \frac{1}{K_{ads}} + C \quad (17)$$

linear fitting of the plots of C/θ against C (Fig. 5 and Fig. S6 in ESI†) corresponds to the correlation coefficient (R^2) of 0.999 and yields slopes nearly equal to unity (Table 5). These results justify the applicability of the Langmuir adsorption isotherm towards the adsorption of BT-Py derivatives on mild steel surfaces in aqueous HCl.[63,64] K_{ads} in eqn (17) is the equilibrium adsorption constant, which is obtained from the intercept of the plots of C/θ *vs.* C. K_{ads} is related to the standard free energy (ΔG^0_{ads}) of adsorption by the following equation:

$$\Delta G^0_{ads} = -RT \ln(55.56\ K_{ads}) \quad (18)$$

where 55.56 is the molar concentration of water.[65,66] Fig. 5 and Fig. S6 in the ESI† expose the identical nature of the adsorption isotherms for an inhibitor at different temperatures, which is reflected in almost the same values of K_{ads} or ΔG^0_{ads} for an inhibitor in the experimental temperature range (Table 5). APYBT has the highest values of K_{ads}. This makes the ΔG^0_{ads} values most negative for APYBT. The ΔG^0_{ads} values for all three inhibitors increase with the temperature and reach almost -40 kJ mol^{-1}. Such a figure is typical for chemisorption and thus reflects a quite strong adsorptive interaction between the BT-Py derivatives and the mild steel surface in an aqueous acidic medium, particularly at relatively higher temperature.[67,68]

When we plot ΔG^0_{ads} against different temperatures, T, a linear variation is observed (Fig. 6) and by fitting the data points following eqn (19), we get the enthalpy of adsorption (ΔH^0_{ads}) and entropy of adsorption (ΔS^0_{ads}) from the intercept and slope, respectively (Table 6).

$$G^0_{ads} = \Delta H^0_{ads} - T\Delta S^0_{ads} \quad (19)$$

Table 5 Adsorption parameters

Inh.	Temp. (K)	R^2	Slope	Intercept	$K_{ads} \times 10^{-3}$ (M^{-1})	$-\Delta G^0_{ads}$ (kJ mol^{-1})
APYBT	293	0.999	1.026	0.0101	98.72	37.80
	303	0.999	1.023	0.0097	102.25	39.18
	313	0.999	1.017	0.0092	108.11	40.62
	323	0.999	1.019	0.0096	103.41	41.80
HPYBT	293	0.999	1.033	0.0182	54.85	36.37
	303	0.999	1.029	0.0175	56.88	37.70
	313	0.999	1.022	0.0169	58.99	39.04
	323	0.999	1.027	0.0172	57.87	40.24
PYBT	293	0.999	1.044	0.0288	34.72	35.25
	303	0.999	1.038	0.0257	38.83	36.74
	313	0.999	1.033	0.0254	39.23	37.98
	323	0.999	1.037	0.0263	37.98	39.11

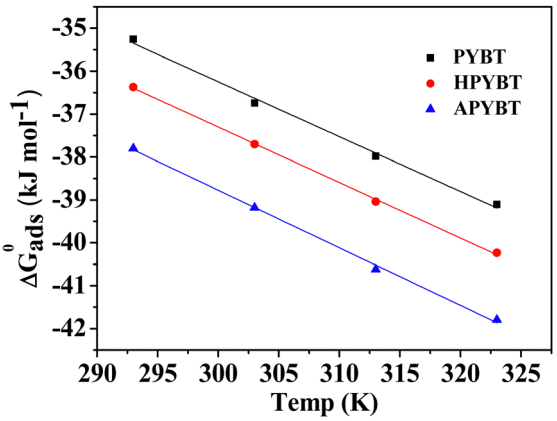

Fig. 6 Plot of ΔG^0_{ads} *vs.* *T*.

Table 6 ΔH^0_{ads} and ΔS^0_{ads} data of the different BT-Py derivatives

	ΔH^0_{ads} (kJ mol^{-1})			ΔS^0_{ads} (J K^{-1} mol^{-1})		
Temp. (K)	APYBT	HPYBT	PYBT	APYBT	HPYBT	PYBT
293–323	1.50	1.52	2.12	134.2	129.4	127.9

A positive value of enthalpy of adsorption signifies an endothermic adsorption. This process involves many associated steps, like initial electrostatic attraction between the protonated heterocyclic base and surface adsorbed Cl^- ions (as it is well documented that mild steel in aqueous HCl solution is positively charged, which attracts the chloride ion onto its surface along with water molecules),[69] and desorption of pre-adsorbed water molecules and Cl^- ions to accommodate the inhibitor molecules on the metal surface. The experimentally obtained enthalpy of adsorption is the average of all of the energy terms associated with these intermediate steps. As this overall enthalpy of adsorption is slightly positive, we can conclude that the energy required for the desorption of the pre-adsorbed water molecules, which is of the order of 100 kJ mol^{-1},[70,71] supersedes the energy release during the adsorption of the inhibitors. The positive value of ΔS^0_{ads}, which reflects enhancement in randomness during the adsorption process, also supports the above conclusion.[72]

Activation parameters

Thermodynamic activation parameters of the uninhibited and inhibited systems are evaluated from the following two equations (eqn (20) and (21)):

$$\log \mathrm{CR} = \log \lambda - \frac{E^*}{2.303RT} \quad (20)$$

$$\mathrm{CR} = \frac{RT}{N_A h} \exp\left(\frac{\Delta S^*}{R}\right) \exp\left(\frac{-\Delta H^*}{RT}\right) \quad (21)$$

Here, CR is the corrosion rate (as obtained from weight loss measurement), λ is the Arrhenius frequency factor, E^* is the activation energy of the corrosion process, N_A is Avogadro's number, R is the universal gas constant, h is Planck's constant, T is the absolute temperature (in Kelvin), and ΔS^* and ΔH^* are the entropy and enthalpy of activation, respectively.

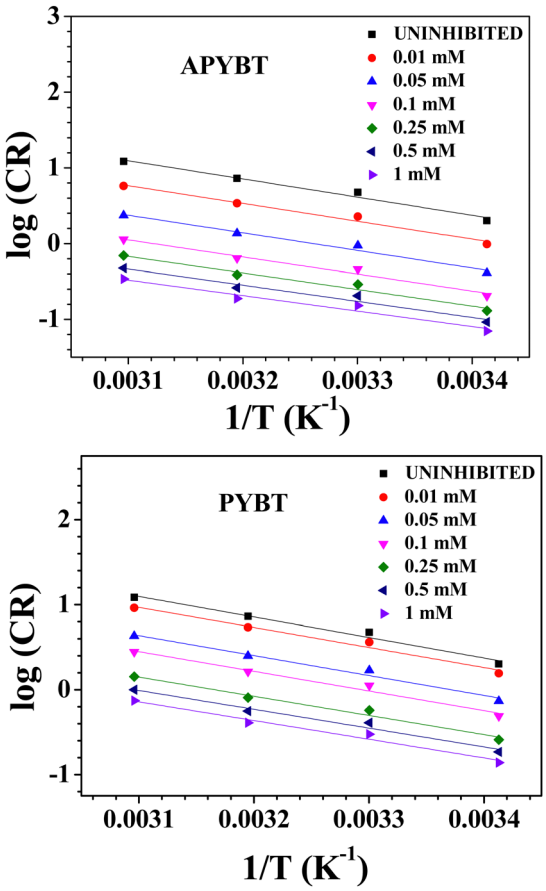

Fig. 7 Arrhenius plots for mild steel in 1 M HCl solution in the absence and presence of APYBT (top) and PYBT (bottom).

The slope and intercept obtained from the plot of log CR *vs.* $1/T$ (Fig. 7 and Fig. S7 in ESI†) yield the values of E^* and λ, respectively. The ΔS^* and ΔH^* values are obtained from the plot of log(CR/*T*) *vs.* $1/T$ [(Fig. S8(A–C) in ESI†]. All thermodynamics activation parameters obtained are tabulated in Table 7. Inspection of the table reveals that with increasing inhibitor concentration, the values of both λ and E^* decrease and are minimum at 1 mM concentration. Similarly, ΔH^* also decreases with concentration. The reduction in the rate of the hydrogen evolution reaction on the increasingly organic inhibitor-coated surface, in spite of the decrease in the activation energy, is indicative of the strong bonding of the organic inhibitor on the metal surface (*i.e.*, chemisorption).[73] This will provide hindrance to the rate determining intermediate step of the hydrogen evolution reaction (HER), *i.e.*, either the Volmer or Heyrovsky intermediate step associated with the HER (eqn (22)–(24)).[74]

$$\text{Volmer step: } [(H_2O)_n - H]^+ + e + M \rightleftharpoons M - H + (H_2O)_n \quad (22)$$

Table 7 Activation parameters for the corrosion of mild steel in 1 M HCl with and without inhibitors

Inhibitors	Conc. (mM)	$\lambda \times 10^{-6}$ (mg cm^{-2} h^{-1})	E^* (kJ mol^{-1})	ΔH^* (kJ mol^{-1})	ΔS^* (J K^{-1} mol^{-1})	$E^* - \Delta H^*$ (kJ mol^{-1})
Uninhibited	0	358.23	46.07	43.51	−89.74	2.56
APYBT	0.01	116.14	45.08	42.53	−99.11	2.56
	0.05	37.19	44.45	41.89	−108.58	2.56
	0.10	10.52	43.07	40.52	−119.08	2.56
	0.25	3.97	41.80	39.24	−127.19	2.56
	0.50	1.79	40.70	38.15	−133.78	2.56
	1.00	0.70	39.09	36.53	−141.58	2.56
HPYBT	0.01	175.15	45.33	42.78	−95.69	2.56
	0.05	58.67	44.74	42.18	−104.79	2.56
	0.10	22.45	43.96	41.41	−112.78	2.56
	0.25	9.62	42.98	40.43	−119.82	2.56
	0.50	6.57	42.76	40.21	−122.99	2.56
	1.00	1.93	40.83	38.28	−133.17	2.56
PYBT	0.01	181.77	45.04	42.49	−95.38	2.56
	0.05	79.17	44.86	42.30	−102.29	2.56
	0.10	41.15	44.27	41.71	−107.74	2.56
	0.25	13.98	43.22	40.66	−116.71	2.56
	0.50	7.23	42.42	39.86	−122.20	2.56
	1.00	4.80	42.15	39.59	−125.61	2.56

$$\text{Heyrovsky step: } M - H + [(H_2O)_n - H]^+ e \rightleftharpoons H_2 + (H_2O)_n + M \quad (23)$$

$$\text{Tafel step: } 2M - H \rightleftharpoons H_2 + 2M \quad (24)$$

Such hindrance will decrease the pre-exponential factor or frequency factor value with enhanced inhibitor concentration. The entropy of activation (ΔS^*) is negative for the uninhibited and inhibited solutions, reflecting more orderliness of the activated complex associated with the Volmer or Heyrovsky intermediate step of the HER. Furthermore, ΔS^* is found to be even more negative from the uninhibited sample. As the inhibitor blocks the cathodic reaction sites by an appreciable extent, proton adsorption on the metal surface or recombining surface adsorbed hydrogen atoms requires closer interaction, resulting in a more negative ΔS^* value. Consistency in the calculated values of E^* and ΔH^* is established from their difference ($E^* - \Delta H^*$). This is constant for all inhibitor systems and the value is 2.56 kJ mol^{-1} which is equal to the room temperature energy (RT) at 308 K, *i.e.*, the mean of the experimental range of temperature used in the present study.

The occurrence of the Volmer or Heyrovsky intermediate step as the possible rate determining step for the HER can also be interpreted from the cathodic Tafel slope values, which are within a range of −90 mV to −130 mV per decade in the present case.[39,49]

SEM morphology

Fig. 8 represents the images of the mild steel surface immersed in 1 M HCl solution without and with 1 mM concentration of inhibitors (immersion time 24 h). Without an inhibitor, the mild steel is seen to encounter heavy corrosion. However, the BT-Py derivatives protect the mild steel from acid corrosion to an appreciable extent. This is a visual confirmation of the effectiveness of the studied molecules as corrosion inhibitors

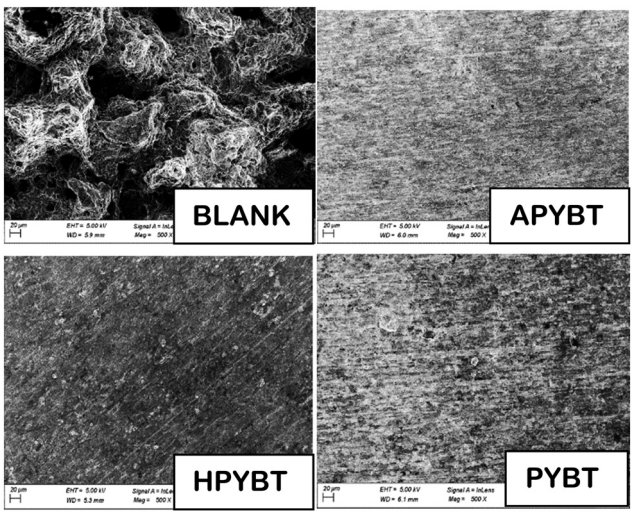

Fig. 8 SEM images of the mild steel surface after immersing it for 24 h at room temperature in the presence and absence of inhibitors.

by providing a barrier film on the mild steel surface in an acid medium. The protective film hinders contact between the mild steel surface and the acid medium and hence reduces the aggressiveness of the latter. Fig. 8 demonstrates that at 1 mM concentration, all three BT-Py derivatives impart comparable corrosion abatement efficacy.

UV-Vis absorption study

UV-Vis absorption spectra of the inhibitor molecules in 1 M aqueous HCl in the absence and presence of mild steel coupons are shown in Fig. 9. We have used 1 mM concentration of the inhibitor in 1 M aqueous HCl. One set of experiments was done without any mild steel coupon. In another, mild steel coupons were immersed in the acidic inhibitor solution for 14 h. The

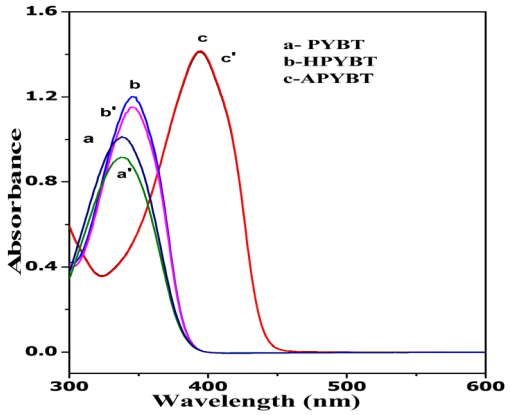

Fig. 9 Absorbance spectra of the inhibitors in 1 M HCl in the absence (a, b, c) and presence of mild steel coupons (a′, b′, c′).

respective spectrum was drawn after proper dilution with 1 M HCl. It is observed that the absorption maximum shifts towards higher wavelength in the presence of substituent groups (bathochromic shift). These absorption maxima correspond to the respective π to π^* transition.[75] It is observed that the absorbance spectrum of a particular inhibitor molecule in 1 M HCl without Fe coupons coincides exactly with that where an Fe coupon is present. In the presence of a mild steel coupon, no additional band at the higher wavelength that may originate from any possible charge transfer between the inhibitor and Fe^{2+} ions is observed. This rules out the possibility of chelation between the inhibitor molecule and Fe^{2+} ion, at least in 1 M HCl medium. Thus, inhibitor film formation should be the primary mechanism for corrosion inhibition in the present case.

Electronic parameters from DFT study

The magnitude of the interaction between the organic inhibitor molecule and metal surface depends on the extent of charge transfer happening between them. From density functional theory calculation, a great deal of information is obtained regarding the reactivity of molecules towards charge transfer reactions. The frontier molecular orbitals are involved in the charge transfer processes, and hence the reactivity largely depends on the energy of these orbitals (HOMO and LUMO). Higher HOMO energy, *i.e.*, lower ionization energy of the organic molecule, will enable the inhibitor molecule to donate an electron to any electrophile. On the other hand, the molecule will be more susceptible to accepting an electron from a nucleophile if it possesses lower LUMO energy, *i.e.*, higher electron affinity. Combining both, the lower the energy gap between the LUMO and HOMO of the inhibitor molecule, the greater its reactivity towards charge transfer.[76] Mild steel acts as both the electrophile and nucleophile, as it can accept an electron from the inhibitor to its vacant 3d orbitals, whereas it can donate an electron from its filled 4s orbitals. Forward electron transfer from inhibitor to metal enhances the electron density on the metal, and this in turn facilitates the retro-electron donation from metal to inhibitor. Thus, the higher the electron transfer from the inhibitor to the metal, the more intricate the interaction between the two. Furthermore, concerning the relation between charge transfer and the mitigation of corrosion processes, it is argued that enhancement of electron density at the anodic reaction sites on the metal will reduce the rate of the anodic metal oxidation reaction; whereas a dearth of electron density at cathodic sites on the metal will deescalate the rate of the cathodic reduction reaction.[39,40] Thus, an inhibitor works in two ways, by blocking the reaction sites reducing the aggressiveness of the corrosive medium (adsorption type inhibitor), and by manipulating the electron availability at anodic and cathodic reaction sites by forward or retro electron transfer (anodic/cathodic inhibitor).[77]

Table 8 Molecular parameters of different BT-Py derivatives as derived from DFT study

Inhibitors	E_{HOMO} (eV)	E_{LUMO} (eV)	ΔE (eV)	χ (eV)	η (eV)	σ (eV^{-1})	ΔN	μ (D)
APYBT	−5.9748	−2.0751	3.8997	4.025	1.949	0.513	0.204	3.51
HPYBT	−6.3307	−2.0586	4.2721	4.195	2.136	0.468	0.146	3.63
PYBT	−6.5938	−2.2169	4.3769	4.405	2.188	0.457	0.095	1.88

The energy of the HOMO is seen to vary in the order PYBT < HPYBT < APYBT (Table 8). Thus, electron transfer from the HOMO of the inhibitor to the metal is the most favourable for APYBT and least for PYBT. For the energy of the LUMO, no definite trend is observed. E_{LUMO} is the lowest for PYBT and almost the same for the other two. Thus, PYBT should be more prone towards electron acceptance from the metal among the three BT-Py derivatives. This whole trend is reflected in the fraction of electrons transferred (ΔN) from inhibitor to metal, which is positive and follows the order: APYBT > HPYBT > PYBT (Table 8). This is consistent with the corrosion inhibition efficiency trend as obtained experimentally. Again, intricate interaction requires the organic inhibitor molecule to possess greater softness.[78] Theoretically calculated order of softness also validates this requirement. For PYBT, the dipole moment is the least. The presence of $-NH_2$ or –OH substituents invokes higher dipole moment for APYBT and HPYBT, which enhances the electrostatic interaction between those molecules and the metal surface.[79] From the optimized geometry of the inhibitor molecules and electronic disposition in the HOMO and LUMO levels, the mode of interaction between the inhibitor and metal is presumed. It is seen that all three BT-Py derivatives are almost planar (Fig. 10). Furthermore, the electron density in the HOMO and LUMO levels are almost similarly distributed over the whole molecular surface (Fig. 10). Thus, it can be said that the interaction pattern of the BT-Py derivatives with the metal surface is quite identical; the total molecular backbone is engaged to facilitate bi-directional charge transfer.

Fukui indices analysis

To provide an atomistic analysis of the mode of interaction, Fukui indices of each atom present in the inhibitor molecules are evaluated. The values of f_k^+ and f_k^- of the C atoms of the benzene ring of BT are almost comparable, suggesting that C atoms engaged in the aromatic ring are involved in both

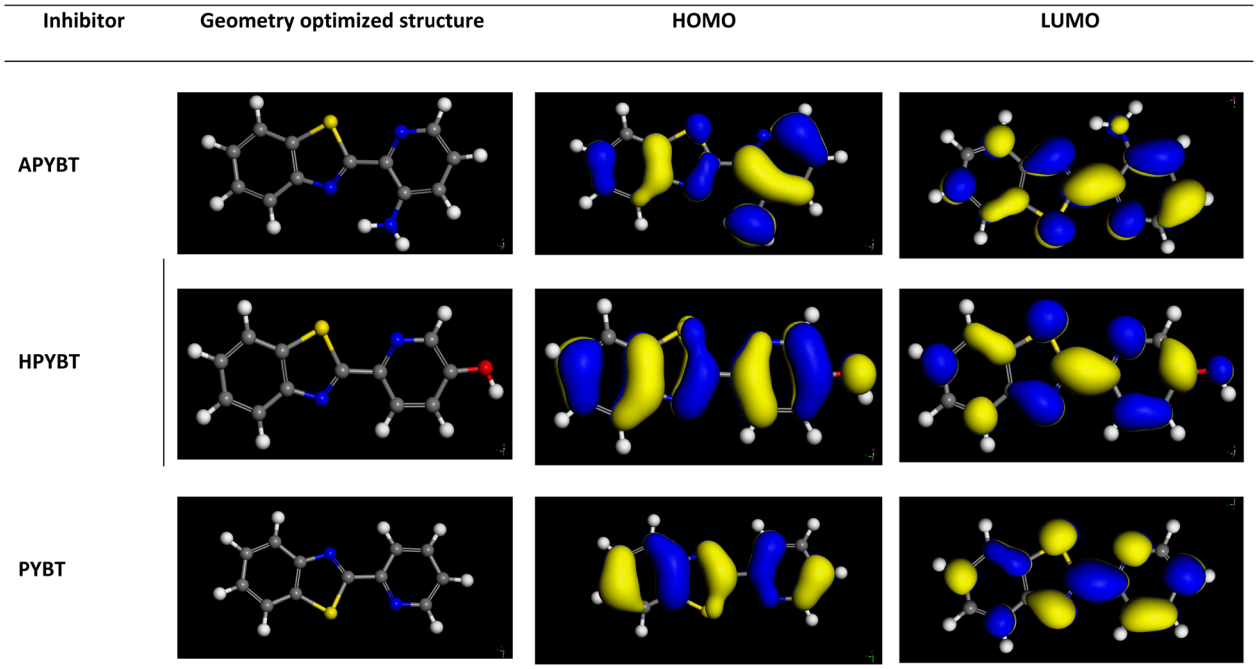

Fig. 10 Electronic distribution in the HOMO and LUMO for the studied BT-pyridine derivatives.

electron donation to the metal, as well as acceptance. Heteroatoms present in the benzothiazole ring, *i.e.*, N and S, possess a relatively higher value of f_k^+ over that of f_k^-. Thus, the N and S atoms of the benzothiazole are more inclined towards electron acceptance from the metal through their vacant (2p for N) or (3d for S) orbitals. The same conclusion can be drawn for the C atom connecting BT and Py moieties (C7). The C atoms of the pyridine ring also have comparable f_k^+ and f_k^- values, some exhibiting slightly higher f_k^+ value, whereas others possess a relatively higher value of f_k^-. The N atom of the pyridine moiety, on the other hand, shows a definite trend for all three molecules; the f_k^+ values are definitely larger than the f_k^- values. Regarding the heteroatom present in the substituted group attached to the pyridine ring, *i.e.*, N atom of APYBT and O atom of HPYBT, it is the f_k^- value that exceeds that of f_k^+. It may thus be concluded that the aromatic pi-systems of BT and Py rings are engaged in bi-directional electron transfer, whereas the heteroatoms present in those systems are relatively inclined towards electron acceptance. The substituted groups attached to the pyridine ring in APYBT and HPYBT are mostly involved in electron donation. The higher f_k^- of the N atom of the amine group of APYBT than that of the O atom of the hydroxyl group of HPYBT makes APYBT a better candidate towards interacting with the metal surface through electron donation. Based on the above argument, the possible mode of interaction between

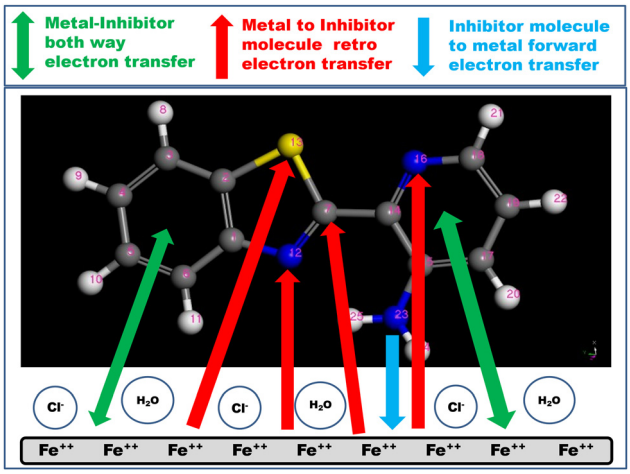

Scheme 2 Mode of adsorption of APYBT with the metal surface following DFT calculation.

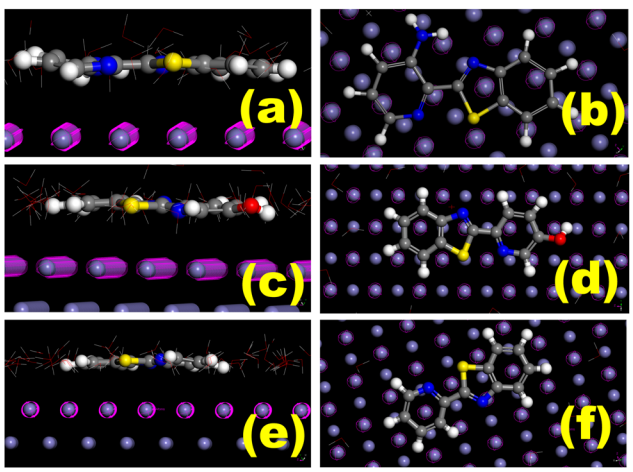

Fig. 11 Orientation of APYBT (a and b), HPYBT (c and d) and PYBT (e and f) in the presence of an Fe surface as obtained from MD simulation study.

Table 9 Interaction energy between the Fe (110) surface and inhibitor molecules as obtained from MD simulation study

System	$E_{interaction}$ (kJ mol^{-1})	$E_{interaction}$ (kcal mol^{-1})
Fe (110) + APYBT	−440.2	−105.2
Fe (110) + HPYBT	−412.1	−98.5
Fe (110) + PYBT	−233.5	−55.8

APYBT and the Fe surface is schematically represented in Scheme 2.

In addition to the above generalization, more intricate details on the role of the substituent towards the relative electron acceptance–donation property of the BT and Py units can be evaluated from the ratio $\left(\frac{f_k^+}{f_k^-}\right)$. The corresponding value for the S atom of the BT ring in PYBT is 1.27, whereas that in HPYBT is 1.5 and it is 1.45 in the case of APYBT. The same ratio for the N atom of the BT ring in PYBT is 1.6. This increases to 1.87 in the case of HPYBT and 1.62 for APYBT. Similar inference can be drawn for the C atoms present in the BT ring (C1 to C7). Thus, the presence of the substituent enhances the electron acceptance capacity of the BT ring as a whole. In the Py moiety, the opposite trend is observed. The ratio $\left(\frac{f_k^+}{f_k^-}\right)$ for the N atom of the Py group in PYBT is 2.2, whereas it is 1.86 and 2 for HPYBT and APYBT, respectively. Thus, the electron donation property of the ring N atom in the Py moiety is enhanced in the presence of substituents attached to the Py ring. When the substituent groups are attached to the Py ring, the ratio $\left(\frac{f_k^+}{f_k^-}\right)$ not only decreases for the pyridine N atom, but also for the ring C atoms. Thus, it may be concluded that the electron donating substituent (–NH_2 or –OH) triggers the electron donating property of the Py moiety.

MD simulation result

From MD simulation, the adsorption pattern of the studied BT-Py derivatives on the metal surface can be visualized. The molecules are seen to interact in a parallel orientation with the Fe surface (Fig. 11).

The distances among the atoms present in the inhibitor molecules (C, N, O or S) and the Fe atoms of the uppermost layer are in a range of 2.8–3.3 Å (Fig. S10 in ESI†). This exemplifies the strength of the interaction of the inhibitor molecules with the Fe surface, replacing the surface adsorbed water molecules. As suggested in the literature, the observed interaction distance is a manifestation of chemisorption for the

Table 10 Comparative table on the IE of various benzothiazole and pyridine derivatives

Inhibitor	Conc.	System	%IE	Ref.
2-Mercaptobenzothiazole	2 mM	Carbon steel in 1 M HCl	86	24
2-Aminobenzothiazole	2 mM		78	
Benzothiazole-2-amine	5 mM	Mild steel in 1 M H_2SO_4	83	25
Benzothiazole-2-yl-thiocarbohydrazide			91	
Benzothiazole-2-yl-thiosemicarbazide			91	
6-(4-Chlorophenyl)benzo[*d*]thiazol-2-amine	0.33 mM	Mild steel in 1 M HCl	77	26
6-(*p*-tolyl)benzo[*d*]thiazol-2-amine			88	
6-(4-Methoxyphenyl)benzo[*d*]thiazol-2-amine			97	
2-Amino benzothiazole	500 ppm	Mild steel in 1 M HCl	97	27
2-Amino-6-chloro-benzothiazole			96	
2-Amino-6-methoxy-benzothiazole			86	
2-Amino-6-methyl-benzothiazole			77	
(*Z*)-5-(4-chlorobenzylidene)-3-(benzo[*d*]thiazol-2-yl)-2-(4-methoxyphenyl) thiazolidine-4-one (CBTMT)	150 ppm	Mild steel in 15% HCl	95	29
(*Z*)-5-(4-methoxybenzylidene)-3-(benzo[*d*]thiazol2-yl)-2-(4-methoxyphenyl)thiazolidine-4-one (MBTMT)			94	
(*E*)-*N*-(Benzo[*d*]thiazol-2-yl)-1-phenylmethanimine	40 ppm	Carbon steel in 1 M HCl	79	30
(*E*)-*N*-(6-Methylbenzo[*d*]thiazol-2-yl)-1-phenylmethanimine			82	
(*E*)-2-(Benzylideneamino)benzo[*d*]thiazole-6-thiol			90	
2-Amino-5-((4-chlorophenyl)diazenyl)pyridin-4-ol	1 mM	Carbon steel in 1 M HCl	78	32
2-Amino-5-(*p*-tolyldiazenyl)pyridin-4-ol			81	
2-Amino-5-((4-methoxyphenyl)diazenyl)pyridin-4-ol			86	
2-Amino-5-((3-nitrophenyl)diazenyl)pyridin-4-ol			70	
Oxazole derivatives of pyridine	300 ppm	Mild steel in 0.5 mM HCl	90	33
(2*Z*)-3-Imino-4-methyl-2-(pyridin-3-ylhydrazono)pentanenitrile	0.1 mM	Carbon steel in 2 M HCl	69	35
4-(3,4-Dichlorophenyl)-2,6-dimethyl-1,2-dihydropyridine-3,5-dicarbonitrile			75	
1,4-Diamino-5-cyano-2-(4-methoxyphenyl)-6-oxo1,6-dihydropyridine-3-carboxylic acid			82	
Ethyl 4-amino-5-cyano-2-(dicyanomethylene)-6-phenyl-1,2-dihydropyridine-3-carboxylate			91	

present kind of system (*i.e.*, adsorption of an organic molecule on the metal surface in aqueous solution).[80] The interaction energy as obtained in MD simulation is completely in agreement with the corrosion inhibitory performance of the studied BT-Py derivatives (Table 9). The interaction energy of APYBT is almost twice that of PYBT, which validates the experimentally obtained result that APYBT acts as a much superior inhibitor than PYBT. The corrosion inhibition efficacies of APYBT and HPYBT are very close, which is also reflected in the interaction energy values.

Comparison of the inhibitive effect with various reported benzothiazole derivatives and other reported pyridine derivatives

The corrosion-inhibitory effects of the researched BT-Py derivatives are compared with various reported benzothiazole derivatives and other reported pyridine derivatives (Table 10). It can be noted that the BT-Py derivatives used in the present study impart higher inhibition efficiency compared to most of the previously reported benzothiazole derivatives and pyridine derivatives.

Conclusion

A comparative account of the anti-corrosion behaviour of pyridine-substituted benzothiazole (BT-Py) derivatives is presented. Both electrochemical and weight loss techniques establish the amino pyridine-substituted BT (APYBT) as a better inhibitor over the hydroxy pyridine-substituted BT (HPYBT). This is attributed to the better electron donating ability of the amino group compared to that of the hydroxy group. APYBT bestows above 97% corrosion inhibition efficiency for mild steel exposed to 1 mM aqueous HCl for 6 h in the temperature range 40–50 °C. The adsorption of BT-Py derivatives on mild steel in acidic solution is essentially chemisorption at elevated temperature as supported from free energy of adsorption data as well as analysis of activation parameters associated with the corrosion kinetics. Though the inhibitors are seen to block both the cathodic and anodic reaction sites on the metal surface, replacing the surface adsorbed water molecules, the inhibitory effect of the cathodic reaction is more obvious. The inhibitory trend of the BT-Py derivatives is aptly justified from various intrinsic electronic parameters obtained from DFT calculations. These include the energies of the frontier molecular orbitals (HOMO and LUMO), molecular hardness and softness, fraction of electron transfer and dipole moment of the inhibitor molecules. A model of bi-directional electron transfer (inhibitor to metal and *vice versa*) involving the whole molecular surface is better suited to corroborate the experimental and theoretical results. The interaction energy between the BT-Py derivatives and the metal surface, as obtained from MD simulation, is completely in line with the experimentally observed inhibitory performance. The minimum distance between the inhibitor molecules and the metal surface in the presence of an aqueous acid solution is found to be 2.8–3.3 Å. This reflects the ability of BT-Py derivatives to interact closely with the mild steel surface.

The present study gives an idea as to how substituents influence the electron donor–acceptor property of atoms present in the inhibitor. The present inhibitor system consists of a BT ring attached to a Py ring. An electron donating substituent ($-NH_2$ or –OH) at the Py ring results in an enhancement of the electron donating ability of the Py moiety, and an overall increase in the electron accepting property of the BT moiety. It will be interesting to study this effect when the BT ring is substituted by such an electron donating group. A similar study may be extended using an electron withdrawing group ($-NO_2$ or –CN *etc.*) also. This will enhance our understanding of the effect of electron donating/accepting substituents at different parts of a complex/conjugated inhibitor molecule.

Author contributions

DS is responsible for conceptualization, funding acquisition, supervision and writing-original draft. AS, SS and RS are responsible for data acquisition and formal analysis. SG and SD are responsible for validation and writing-review and editing.

Conflicts of interest

The authors hereby declare no conflicts of interest.

Acknowledgements

DS and AS thank Department of Science & Technology and Biotechnology, Government of West Bengal, India for supporting research project no. 217(Sanc.)/ST/P/S&T/15G-10/2017 and providing a fellowship. DS thanks SERB, Government of India for providing the computational facility through the project no. EMR/2017/005506.

References

1 H. Assad and A. Kumar, *J. Mol. Liq.*, 2021, **344**, 117755.
2 U. Nazir, Z. Akhter, N. Z. Ali, R. Hussain, F. Liaqat, A. Tahir and S. Qamar, *New J. Chem.*, 2022, **46**, 3925–3938.
3 C. Verma and M. A. Quraishi, *Coord. Chem. Rev.*, 2021, **446**, 214105.
4 A. Dutta, S. K. Saha, U. Adhikari, P. Banerjee and D. Sukul, *Corros. Sci.*, 2017, **123**, 256–266.
5 C. Verma, E. E. Ebenso and M. A. Quraishi, *J. Mol. Liq.*, 2020, **316**, 113874.
6 C. Verma, L. O. Olasunkanmi, E. E. Ebenso and M. A. Quraishi, *J. Mol. Liq.*, 2018, **251**, 100–118.
7 D. A. Winkler, M. Breedon, A. E. Hughes, F. R. Burden, A. S. Barnard, T. G. Harvey and I. Cole, *Green Chem.*, 2014, **16**, 3349–3357.
8 A. Dehghani, G. Bahlakeh and B. Ramezanzadeh, *J. Mol. Liq.*, 2019, **282**, 366–384.

9 A. M. El-Shamy and S. M. Mouneir, *J. Bio- Tribo-Corros.*, 2023, **9**, 3.
10 J. N. Pejić, B. V. Jegdić, B. M. Radojković, D. D. Marunkić, A. D. Marinković and J. B. Bajat, *Corros. Sci.*, 2022, **209**, 110815.
11 R. Farahati, A. Ghaffarinejad, S. M. Mousavi-Khoshdel, J. Rezania, H. Behzadi and A. Shockravi, *Prog. Org. Coat.*, 2019, **132**, 417–428.
12 A. Suhasaria, M. Murmu, S. Satpati, P. Banerjee and D. Sukul, *J. Mol. Liq.*, 2020, **313**, 113537.
13 Z. Chen, L. Huang, G. Zhang, Y. Qiu and X. Guo, *Corros. Sci.*, 2012, **65**, 214–222.
14 T. Yan, S. Zhang, L. Feng, Y. Qiang, L. Lu, D. Fu, Y. Wen, J. Chen, W. Li and B. Tan, *J. Taiwan Inst. Chem. Eng.*, 2020, **106**, 118–129.
15 A. Dutta, S. K. Saha, P. Banerjee and D. Sukul, *Corros. Sci.*, 2015, **98**, 541–550.
16 L. Guo, S. T. Zhang, T. M. Lv and W. J. Feng, *Res. Chem. Intermed.*, 2015, **41**, 3729–3742.
17 D. Dwivedi, K. Lepková and T. Becker, *RSC Adv.*, 2017, **7**, 4580–4610.
18 S. Prakash, G. Somiya, N. Elavarasan, K. Subashini, S. Kanaga, R. Dhandapani, M. Sivanandam, P. Kumaradhas, C. Thirunavukkarasu and V. Sujatha, *J. Mol. Struct.*, 2021, **1224**, 129016.
19 E. Chugunova, C. Boga, I. Sazykin, S. Cino, G. Micheletti, A. Mazzanti, M. Sazykina, A. Burilov, L. Khmelevtsova and N. Kostina, *Eur. J. Med. Chem.*, 2015, **93**, 349.
20 S. Aiello, G. Wells, E. L. Stone, H. Kadri, R. Bazzi, D. R. Bell, M. F. Stevens, C. S. Matthews, T. D. Bradshaw and A. D. Westwell, *J. Med. Chem.*, 2008, **51**, 5135.
21 N. Herrera Cano, M. S. Ballari, A. G. Lopez and A. N. Santiago, *J. Agric. Food Chem.*, 2015, **63**, 3681.
22 X. J. Zheng, C. S. Li, M. Y. Cui, Z. W. Song, X. Q. Bai, C. W. Liang, H. Y. Wang and T. Y. Zhang, *Bioorg. Med. Chem. Lett.*, 2020, **30**, 127237.
23 S. Saeed, N. Rashid, P. G. Jones, M. Ali and R. Hussain, *Eur. J. Med. Chem.*, 2010, **45**, 1323.
24 H. Jafari, K. Akbarzade and I. Danaee, *Arab. J. Chem.*, 2019, **12**, 1387–1394.
25 K. Parameswari, S. Chitra, A. Selvaraj, S. Brindha and M. Menaga, *Port. Electrochim. Acta*, 2012, **30**, 89–98.
26 S. Sengupta, M. Singh, S. Thakur, B. Pani, P. Banerjee, S. Kaya and A. K. Singh, *J. Mol. Liq.*, 2022, **354**, 118890.
27 M. A. Quraishi, M. A. Wajid Khan, M. Ajmal, S. Muralidharan and S. Venkatakrishna Iyer, *J. Appl. Electrochem.*, 1996, **26**, 1253–1258.
28 M. A. Quraishi, M. A. Wajid Khan, M. Ajmal, S. Muralidharan and S. Venkatakrishna Iyer, *Br. Corros. J.*, 1997, **32**, 72–76.
29 M. Yadav, S. Kumar, N. Kumari, I. Bahadur and E. E. Ebenso, *Int. J. Electrochem. Sci.*, 2015, **10**, 602–624.
30 A. A. Farag, A. M. Eid, M. M. Shaban, E. A. Mohamed and G. Raju, *J. Mol. Liq.*, 2021, **336**, 116315.
31 C. Verma, L. O. Olasunkanmi, I. B. Obot, E. E. Ebenso and M. A. Quraishi, *RSC Adv.*, 2016, **6**, 53933–53948.
32 M. Abdallah, M. M. Alfakeer, N. F. Hasan, A. M. Alharbi and E. M. Mabrouk, *Orient. J. Chem.*, 2019, **35**(1), 98–109.
33 D. M. Gurudatt and K. N. Mohana, *Ind. Eng. Chem. Res.*, 2014, **53**, 2092–2105.
34 R. K. Gupta, M. Malviya, C. Verma, N. K. Gupta and M. A. Quraishi, *RSC Adv.*, 2017, **7**, 39063–39074.
35 S. A. Abd El-Maksoud and A. S. Fouda, *Mater. Chem. Phys.*, 2005, **93**, 84–90.
36 P. Han, W. Li, H. Tian, X. Gao, R. Ding, C. Xiong, L. Song, X. Zhang, W. Wang and C. Chen, *Mater. Chem. Phys.*, 2018, **214**, 345–354.
37 H. El Sayed, A. El Nemr and S. Ragab, *J. Mol. Model.*, 2012, **18**, 1173–1188.
38 C. Verma, K. Y. Rhee, M. A. Quraishi and E. E. Ebenso, *J. Taiwan Inst. Chem. Eng.*, 2020, **117**, 265–277.
39 S. Satpati, A. Suhasaria, S. Ghosal, U. Adhikari, P. Banerjee, S. Dey and D. Sukul, *J. Mol. Struct.*, 2022, **1268**, 133684.
40 S. Satpati, A. Suhasaria, S. Ghosal, S. Dey and D. Sukul, *Mater. Chem. Phys.*, 2023, **296**, 127200.
41 R. G. Parr and R. G. Pearson, *J. Am. Chem. Soc.*, 1983, **105**, 7512.
42 T. Tsuneda, *Int. J. Quantum Chem.*, 2015, **115**, 270.
43 R. Pal and P. K. Chattaraj, *J. Comput. Chem.*, 2023, **44**, 278–297.
44 A. Kokalj and N. Kovačevic, *Chem. Phys. Lett.*, 2011, **507**, 181–184.
45 J. Tan, L. Guo, D. Wu, S. Wang, R. Yu, F. Zhang and S. Kaya, *Int. J. Electrochem. Sci.*, 2020, **15**, 1893–1903.
46 P. Fuentealba, P. Pérez and R. Contreras, *J. Chem. Phys.*, 2000, **113**, 2454.
47 W. Yang and W. J. Mortier, *J. Am. Chem. Soc.*, 1986, **108**, 5708–5711.
48 P. W. Ayers and M. Levy, *Theor. Chem. Acc.*, 2000, **103**, 353–360.
49 S. Satpati, A. Suhasaria, S. Ghosal, A. Saha, S. Dey and D. Sukul, *J. Mol. Liq.*, 2021, **324**, 115077.
50 D. Sukul, A. Pal, S. K. Saha, S. Satpati, U. Adhikari and P. Banerjee, *Phys. Chem. Chem. Phys.*, 2018, **20**, 6562–6574.
51 P. Arellanes-Lozada, V. Díaz-Jiménez, H. Hernández-Cocoletzi, N. Nava, O. Olivares-Xometl and N. V. Likhanova, *Corros. Sci.*, 2020, **175**, 108888.
52 S. A. Umoren, R. K. Suleiman, I. B. Obot, M. M. Solomon and A. Y. Adesina, *J. Mol. Liq.*, 2022, **356**, 119002.
53 C. Cao, *Corros. Sci.*, 1996, **38**, 2073–2082.
54 F. Mansfeld, *Electrochim. Acta*, 1990, **35**, 1533–1544.
55 D. Sukul, A. Pal, S. Mukhopadhyay, S. K. Saha and P. Banerjee, *J. Mol. Liq.*, 2018, **249**, 930–940.
56 A. Tazouti, M. Galai, R. Touir, M. E. Touhami, A. Zarrouk, Y. Ramli, M. Saraçoğlu, S. Kaya, F. Kandemirli and C. Kaya, *J. Mol. Liq.*, 2016, **221**, 815–832.
57 C. M. Fernandes, A. R. Costa, M. C. Leite, V. Martins, H. S. Lee, F. da, C. S. Boechat, M. C. de Souza, P. N. Batalha, H. Lgaz and E. A. Ponzio, *J. Mol. Liq.*, 2023, **375**, 121299.
58 E. A. Hernández-Pagán, N. M. Vargas-Barbosa, T. Wang, Y. Zhao, E. S. Smotkin and T. E. Mallouk, *Energy Environ. Sci.*, 2012, **5**, 7582–7589.

59 W. H. Mulder, J. H. Sluyters, T. Pajkossy and L. Nyikos, *J. Electroanal. Chem. Interfacial Electrochem.*, 1990, **285**, 103–115.
60 A. R. Bredar, A. L. Chown, A. R. Burton and B. H. Farnum, *ACS Appl. Energy Mater.*, 2020, **3**, 66–98.
61 B. Hirschorn, M. E. Orazem, B. Tribollet, V. Vivier, I. Frateur and M. Musiani, *J. Electrochem. Soc.*, 2010, **157**, C458–C463.
62 A. Suhasaria, S. Satpati, S. Ghosal, S. Dey and D. Sukul, *J. Bio- Tribo-Corros.*, 2023, **9**, 26.
63 A. Kokalj, *Corros. Sci.*, 2023, **217**, 111112.
64 E. Ituen, O. Akaranta and A. James, *Chem. Sci. Int. J.*, 2017, **18**, 1–34.
65 Y. Liu, *J. Chem. Eng. Data*, 2009, **54**, 1981–1985.
66 K. Slobodan and A. Milonjic, *J. Serb. Chem. Soc.*, 2007, **72**, 1363–1367.
67 G. Moretti, G. Quartarone, A. Tassan and A. Zlngales, *Electrochim. Acta*, 1996, **41**, 1971–1980.
68 Y. Shi, L. Chen, S. Hou, S. Zhang, X. Wang, P. Dong, F. Gao and H. Li, *Colloids Surf. A Physicochem. Eng. Asp.*, 2023, **656**, 130501.
69 H. L. Kele, M. Kele, L. Dehri and O. Serinda, *Colloids Surf. A Physicochem. Eng. Asp.*, 2008, **320**, 138–145.
70 M. Egashlra, M. Nakashlma, S. Kawasuml and T. Selyama, *J. Phys. Chem.*, 1981, **85**, 4125–4130.
71 H. Kim, H. J. Cho, S. Narayanan, S. Yang, H. Furukawa, S. Schiffres, X. Li, Y. B. Zhang, J. Jiang, O. M. Yaghi and E. N. Wang, *Sci. Rep.*, 2016, **6**, 19097.
72 A. S. Al-Gorair, S. Abd El Wanees, M. A. Hegazy, S. S. Al-Juaid, K. A. Soliman and M. M. Asab, *Mater. Chem. Phys.*, 2023, **297**, 127351.
73 M. Bouklah, B. Hammouti, M. Lagrenée and F. Bentiss, *Corros. Sci.*, 2006, **48**, 2831–2842.
74 A. Lasia, *Int. J. Hydrog. Energy.*, 2019, **44**, 19484–19518.
75 A. Irfan, A. Kalam, A. G. Al-Sehemi and M. Dubey, *Molecules*, 2022, **27**, 8672.
76 Ş. Erdoğan, Z. S. Safi, S. Kaya, D. Ö. Işın, L. Guo and C. Kaya, *J. Mol. Struct.*, 2017, **1134**, 751–761.
77 L. T. Popoola, *Corros. Rev.*, 2019, **37**, 71–102.
78 D. Quy Huong, T. Duong and P. C. Nam, *ACS Omega*, 2019, **4**, 14478–14489.
79 I. Y. Yaagoob, L. K. Goni, M. A. Mazumder, S. A. Ali, M. A. Quraishi and C. Verma, *New J. Chem.*, 2023, **47**, 3445–3461.
80 S. Ravi, S. Peters, E. Varathan and M. Ravi, *Colloids Surf. A Physicochem. Eng. Asp.*, 2023, **661**, 130919.